

## Eccentricity driven comparative analysis of GW source detections with LISA

SYED ALI MOHSIN BUKHARI,<sup>1</sup> NAZEELA AIMEN,<sup>1, 2, 3</sup> ZARNIGAH KAYANI,<sup>1, 4</sup> AND ASAD ALI<sup>1, 2</sup>

<sup>1</sup>*Space and Astrophysics Research Lab (SARL), National Centre of GIS and Space Applications (NCGSA), Islamabad 44000, Pakistan.*

<sup>2</sup>*Department of Applied Mathematics and Statistics, Institute of Space Technology, 1, Islamabad Highway, Islamabad 44000, Pakistan.*

<sup>3</sup>*Department of Statistics, The University of Auckland, Auckland 1142, New Zealand.*

<sup>4</sup>*Department of Space Science, Institute of Space Technology, 1, Islamabad Highway, Islamabad 44000, Pakistan.*

(Received June 1, 2019; Revised January 10, 2019; Accepted August 17, 2023)

Submitted to ApJ

### ABSTRACT

The double compact objects (DCOs) present a broad range of possible GW detections in our MW galaxy. Here we present a case study on the detection of DCOs with progenitors having high metallic content. Furthermore, the effects of eccentricity on the ZAMS stage on the evolution of binaries is also checked via a comparative analysis for two identical data sets. The binaries were generated using the Compact Object Mergers: Population Astrophysics and Statistics (COMPAS) suite, followed by their distribution in a metallicity–age dependent Milky Way galaxy model.

For a 4-year LISA mission, this study predicts a detection rate between 83–124(86–131) detections for data sets with non-zero and zero ZAMS eccentricity respectively. Out of these, 21–45(17–36) are BHBHs, 17–44(17–38) are NSNSs, 6–28(11–29) are BHNSs and 13–39(21–46) are NSBHs. NSBH were considered separate from BHNS as the stellar evolution indicates that the primary star in the binary ended up as a NS instead of a BH. It was also observed that some common binaries end up in different DCO stages in both data sets.

**Keywords:** gravitational waves – gravitational waves detectors – black holes – neutron stars – double compact objects – binary stars

### 1. INTRODUCTION

The gravitational waves (GW) were predicted a year after the final formulation of the general theory of relativity (GR) by Albert Einstein (Einstein 1916). Similar to electromagnetic waves, the GWs travel at the speed of light (Eddington 1922; Abbott et al. 2016). However, unlike electromagnetic waves, the GW stretches and squeezes the space itself thus causing spatial disturbances. The detection of Hulse-Taylor binary (Hulse & Taylor 1975), and the subsequent observation of a seven years time span (Taylor & Weisberg 1982) stirred a great interest in the GW observations. It wasn't until 2015 that the first direct observation of GW was made by LIGO and VIRGO collaborations (Abbott et al. 2016). The lower frequency bound for both the aLIGO and

VIRGO detectors is around 10 Hz (LIGO Scientific Collaboration et al. 2015; Acernese et al. 2015)

The Laser Interferometer Space Antenna (LISA) has three spacecrafts that form a triangle, each side 2.5 million km long (Prince et al. 2002; Robson et al. 2019). Operating in the frequency range of  $1 \times 10^{-5} \text{ Hz} \leq f \leq 1 \times 10^{-1} \text{ Hz}$  LISA will be able to observe the sources millions of years before they merge. The early detection capability will help better constrain and determine the orbital parameters of the observed binaries. Some sources detectable by LISA are the extreme mass ratio inspirals (EMRIs) (Klein et al. 2016; Gair et al. 2017; Chapman-Bird et al. 2022) and galactic binaries (Abbott et al. 2016; Wagg et al. 2022b; Digman & Hirata 2022). This makes LISA also capable of mapping Milky Way galaxy's structure. Another interesting class detectable by LISA is the double white dwarf stars (DWDs) which are reported to be abundant in our MW galaxy and have a substantial detection in LISA as well (Nelemans et al.

2001; Willems et al. 2007; Ruiter et al. 2010; Korol et al. 2017).

A lot of effort has been put into the detection of potential GW sources for LISA, the resolution of issues that might be associated with the background data, and proposals of new candidates as GW sources for LISA (see, for example, Nelemans et al. 2001; Babak et al. 2008; Sesana et al. 2009; Babak et al. 2010; Belczynski et al. 2010; Blaut et al. 2010; Ruiter et al. 2010; Yu & Jeffery 2010; Guo et al. 2017; Khakhaleva-Li & Hogan 2020; Lau et al. 2020; Broekgaarden et al. 2021; Shao & Li 2021; Renzo et al. 2021; Andrews et al. 2020; Fumagalli et al. 2022; Wagg et al. 2022b). The detections of these sources will provide us with a better understanding of not only the evolution phases but also the endpoints of stellar evolution.

The goals of this research are,

1. to predict the number of DCO binaries that can be detected via LISA in our Milky Way galaxy,
  - (a) to determine whether extra galactic sources are LISA detectable,
2. to make a general detection comparison between DCO binaries with and without an initial eccentricity.

This research paper is structured as follows, in section 2 we discuss the generation of binary systems using COMPAS suite. In section 3 we give a general overview of the methodology adopted in this research for evolving the stars from ZAMS to DCOs, from DCOs to merger stage, and their detection by LISA as well. The evolution of binaries and their detection is discussed in section 4.

## 2. POPULATION SYNTHESIS

The population synthesis for the detections of the double compact objects (DCOs) was performed using the Compact Object Mergers: Population Astrophysics and Statistics (COMPAS; Stevenson et al. (2017); Vigna-Gómez et al. (2018); Riley et al. (2022)) suite. COMPAS is a rapid stellar evolution suite and can evolve both single and binary stars following the details outlined by Hurley et al. (2000, 2002). A list of selected papers that make use of the COMPAS suite is also available on the COMPAS website.<sup>1</sup>

This study makes use exclusively of the binary star evolution (BSE) synthesis method. The default parameters used by the COMPAS software are listed in table 1 in the COMPAS paper (Riley et al. 2022).

Except for supernova mass remnant prescription, initial eccentricity ( $e_i$ ), metallicity ( $z$ ), and pulsar evolution, all other parameters were taken at the default value. For a one-to-one correspondence between the two generated data sets, the seed numbers were kept constant.

For the mass of primary star, we draw the values from Kroupa initial mass function (IMF) with  $m_1 \in [5, 150] M_{\odot}$  (Kroupa 2001). For the secondary star, we randomly draw from uniform distribution to satisfy  $q \equiv m_2/m_1$ , where  $q \in [0, 1]$  (Sana et al. 2012). An additional constraint of  $m_2 \geq 0.1 m_1$  was placed on  $m_2$  as this is the minimum mass necessary for a star to be considered as a main sequence star.

For the semi-major axis of the binary, we drew the parameter values from a flat-in-the-log distribution with  $a_i \in [0.1, 1000] \text{ AU}$ , such that  $p(a_i) \propto 1/a_i$  (Öpik 1924).

For the remnant mass prescription, we first considered the Fryer delayed model (Fryer et al. 2012). However, this resulted in a concentration of NS mass around  $\sim 1.28 M_{\odot}$ . To avoid this we used Müller & Mandel prescription (M&M; Mandel & Müller 2020). M&M is a stochastic remnant mass model that offers a smoother mass distribution for NS. We also switched the `evolve_pulsar` flag to **True** during population synthesis.

For metallicity, we drew the values from a Beta(5, 80) distribution. The main motivation behind the selection of such biased distribution is the higher metallic content of present-day stars. The population III stars were primarily composed of pure hydrogen and their deaths produced heavier metals in the Universe. By this extension, the stars that are present now or those that will merge now must have higher metallic content. As such, we also speculate that having stars with higher metallic content might produce more NSNS or NS–BH pairs for detection rather than BHBH pairs.

For eccentricity, we make use of two cases,

- Case I: All the binary systems are generated using a uniform distribution,  $e \in (0, 1]$ .
- Case II: All the binary systems are generated with circular orbits, i.e.,  $e = 0$ .

From here on the data set for Case I and Case II will be represented by  $\Theta_1$  and  $\Theta_2$  respectively. Details about the selection of metallicity and eccentricity values in COMPAS are provided in appendix A.

## 3. EVOLUTION METHODOLOGY

We first generated  $1 \times 10^7$  values for metallicity using the beta distribution within the COMPAS limits. We

<sup>1</sup> <https://compas.science/science.html>

denote the zero-age main sequence (ZAMS) parameters of the binaries as,

$$m_{1\text{ZAMS}}, m_{2\text{ZAMS}}, a_{\text{ZAMS}}, e_{\text{ZAMS}}, Z, \phi \quad (1)$$

COMPAS evolves the binaries up to 13.7 Gyr. We represent the resulting double compact object (DCO) parameters as,

$$m_{1\text{DCO}}, m_{2\text{DCO}}, a_{\text{DCO}}, e_{\text{DCO}}, t_{\text{evolve}}, Z, \phi, \quad (2)$$

where  $Z$  is the metallicity of the binary system,  $\phi$  is the seed number,  $t_{\text{evolve}}$  is the time required to form DCO from ZAMS.  $a_{\text{ZAMS}}$ ,  $a_{\text{DCO}}$ ,  $e_{\text{ZAMS}}$ , and  $e_{\text{DCO}}$  are the semi-major axis and eccentricity of the binary orbit at ZAMS and DCO formation respectively.

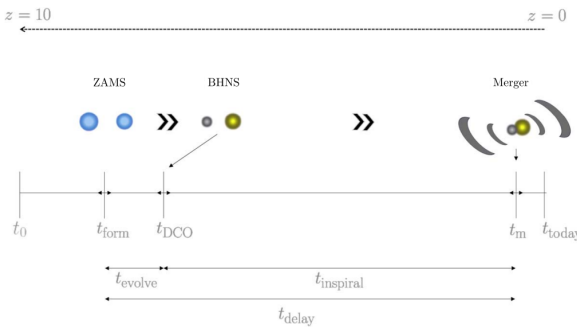


**Figure 1.** Schematic diagram showing various time intervals for a binary system from ZAMS formation, to DCO, and merger. The figure is taken from Riley et al. (2022).

Once the DCOs have been formed, we move out of the COMPAS suite. For the LISA detection, the DCO formed from the set of binaries were checked for an evolutionary stop, i.e., only those binaries were selected that will merge within the Hubble time. The selected candidates were then provided to the python framework LEGWORK (Wagg et al. 2022a) that evolved them from the DCO stage to the merger state. It evolved the binaries using equations from Peters & Mathews (1963); Peters (1964).

The DCO–merger evolution method follows the one outlined by Wagg et al. (2022b) closely with minor changes. The evolution was done such that the MW galaxy instance was divided into bins based on the metallicity values of the evolving binaries. If a binary, at DCO stage, had a resultant merger time<sup>2</sup> greater than the difference of its lookback time<sup>3</sup> and ZAMS-DCO evolution time<sup>4</sup>, it was marked as an inspiralling

binary. Each inspiralling binary was then evolved at every point within the corresponding metallicity bin using LEGWORK to a million year before it merges. At this stage, the resulting LISA parameters of interest were,

$$a_{\text{LISA}}, e_{\text{LISA}}, f_{\text{LISA}} \quad (3)$$

The SNR was then calculated by further evolving them for the LISA mission duration of four years. The detection is made based on the signal-to-noise ratio (SNR) of the binary averaged over sky position, polarization, and orientation using the following expression from (Finn & Thorne 2000),

$$\rho^2 = \sum_{n=1}^{\infty} \int_{f_{n,i}}^{f_{n,f}} \frac{h_{c,n}^2}{f_n^2 S_n(f_n)} df_n, \quad (4)$$

where  $n$  is the GW harmonic,  $f_n$  represents the orbital frequency of  $n^{\text{th}}$  harmonic. The parameter  $S_n(f_n)$  is the LISA sensitivity curve function (Robson et al. 2019), and  $h_{c,n}$  is the characteristic strain of the  $n^{\text{th}}$  GW harmonic (Barack & Cutler 2004).

$$h_{c,n}^2 = \frac{2^{5/3}}{3\pi^{4/3}} \frac{(G\mathcal{M}_c)^{5/3}}{c^3 D_L^2} \frac{1}{f_{\text{orb}}^{1/3}} \frac{g(n,e)}{n F(e)} \quad (5)$$

#### 4. EVOLUTION AND DETECTION

After running the simulations as outlined in section 2, we obtained 12254 DCOs ( $\sim 0.12254\%$ ). Following section 3, we obtain the required parameter values of only 6539 DCOs that merged within Hubble time ( $\sim 53.3621\%$ ) thus making them a potential LISA source.<sup>5</sup> The Hubble time merge rate of DCOs is given in table 1,

**Table 1.** **RowI** shows the merging (M) vs total (T) formed DCOs in this study, **RowII** shows the uniquely detectable (D) vs the merging (M) DCOs from this study for  $\Theta_1$ .

Type	BHBH	NSNS	BHNS	
			NSBH	BHNS
M / T	492 / 663	4752 / 9219	480 / 868	815 / 1504
D / M	348 / 492	1281 / 4752	300 / 480	327 / 815

The highest merging rate in this study is of BHBH pairs ( $\sim 74.21\%$ ), followed by NSBH pairs

<sup>2</sup> Obtained via LEGWORK framework.

<sup>3</sup> Obtained via galaxy synthesis.

<sup>4</sup> Obtained via COMPAS.

<sup>5</sup> Overall, only  $\sim 0.06539\%$  binary system formed into DCOs that merge within Hubble time.

( $\sim 55.30\%$ ), BHNS ( $\sim 54.19\%$ ) and lastly NSNS DCO type ( $\sim 51.55\%$ ) comprising the ‘candidate binaries’, see table 1 **RowI**. ‘Candidate binaries’ were such DCO pairs which can had a potential for detection by LISA at a later evolutionary phase.

Using LEGWORK (Wagg et al. 2022a), these binaries were than checked for their inspiral phase using the  $t_{\text{evolve}}$  and  $t_{\text{lookback}}$  as discussed previously. The difference between lookback and evolution time of a binary was required to be less than its merger time. Out of the merging binaries, BHBH pairs had the most detectable sources in the data set, ( $\sim 70.73\%$ ), followed by NSBH

pair ( $\sim 62.5\%$ ), BHNS pair ( $\sim 40.12\%$ ) and lastly NSNS pair ( $\sim 26.96\%$ ), see table 1 **RowII**.

As the number of detectable binaries in our study was small compared to the total generated population,<sup>6</sup> multiple detections of a single binary object are present in the final output. Table 2 shows selective details about mass of progenitor and their evolutionary ends for maximum and minimum mass at ZAMS and DCO stages. In appendix C we present the number of detection and mean values for selected parameters<sup>7</sup> across the hundred instances of MW galaxies. The number of detections across all the MW instances came out to be 12841.

**Table 2.** Maximum and minimum values for masses of both ZAMS and DCO type stars in the BHBH data set with their respective counterparts. The ‘MAX’ and ‘MIN’ columns represent the maximum and minimum value for the given parameter respectively. The ‘ZAMS details’ and ‘DCO details’ column list the value of primary and secondary components of the binary and respective stage of evolution. All the masses are given in units of solar mass.

Parameters	MAX	ZAMS details		DCO details		MIN	ZAMS details		DCO details	
		Primary	Secondary	Primary	Secondary		Primary	Secondary	Primary	Secondary
<b>Binary Black Holes</b>										
$m_{1\text{ZAMS}}$	149.836	149.836	115.624	10.386	10.395	13.007	13.007	12.500	2.216	2.601
$m_{2\text{ZAMS}}$	131.178	148.802	131.178	8.662	8.459	12.500	13.007	12.500	2.216	2.601
$m_{1\text{DCO}}$	43.308	57.334	57.334	43.308	43.308	2.022	26.497	26.493	2.022	7.104
$m_{2\text{DCO}}$	43.308	57.334	57.334	43.308	43.308	2.018	42.088	30.574	7.456	2.018
<b>Binary Neutron Stars</b>										
$m_{1\text{ZAMS}}$	54.41	54.41	13.76	1.614	1.235	8.546	8.546	7.822	1.26	1.193
$m_{2\text{ZAMS}}$	25.571	25.586	25.571	1.480	1.693	6.626	13.01	6.626	1.26	1.194
$m_{1\text{DCO}}$	1.938	14.022	13.938	1.938	1.487	1.135	10.319	10.019	1.135	1.392
$m_{2\text{DCO}}$	1.991	13.919	13.574	1.681	1.991	1.132	11.674	11.021	1.518	1.132
<b>Neutron Star – Black Hole</b>										
$m_{1\text{ZAMS}}$	53.708	53.708	29.613	1.439	15.342	8.971	8.971	8.847	1.260	3.869
$m_{2\text{ZAMS}}$	42.242	42.289	42.242	1.598	7.382	8.665	9.164	8.665	1.260	2.062
$m_{1\text{DCO}}$	1.935	14.090	13.959	1.935	3.825	1.137	27.186	17.676	1.137	9.646
$m_{2\text{DCO}}$	15.342	53.708	29.613	1.439	15.342	2.003	12.472	12.033	1.608	2.003
<b>Black Hole – Neutron Star</b>										
$m_{1\text{ZAMS}}$	145.467	145.467	46.439	9.907	1.593	11.626	11.626	11.608	2.216	1.522
$m_{2\text{ZAMS}}$	108.489	140.091	108.489	12.217	1.415	10.072	23.144	10.072	2.922	1.206
$m_{1\text{DCO}}$	15.106	90.844	76.11	15.106	1.669	2.004	13.125	12.872	2.004	1.785
$m_{2\text{DCO}}$	1.945	29.142	15.445	4.341	1.945	1.141	28.317	22.834	5.61	1.141

<sup>6</sup> Due to not using any technique that forces DCO production, e.g., STROOPWAFEL Broekgaarden et al. (2019).

<sup>7</sup> The selected parameters include,  $m_{1\text{DCO}}$ ,  $m_{2\text{DCO}}$ ,  $a_{\text{DCO}}$ ,  $e_{\text{DCO}}$ ,  $Z$ ,  $t_{\text{evol}}$ ,  $t_{\text{lookback}}$ , and SNR.

#### 4.1. SNR based source detection

The predicted distribution of the LISA detectable sources is plotted over LISA’s expected sensitivity curve (Robson et al. 2019), in figure 2. The x-axis shows the dominant frequency, the frequency accumulating the largest SNR, for the eccentric binaries. Furthermore, on y-axis we plot the amplitude spectral density (ASD),

including the contribution from all harmonics. The gap between the detected binaries and the LISA curve in the graph is the SNR criteria, ( $\text{SNR} > 7$ ). The size of the points varies with metallicity; high metallic sources have larger shapes and vice versa. The color scheme is based on the eccentricity of detected binaries with a reverse red-yellow-green color palette<sup>8</sup>, going from green, yellow and finally red in increasing order of eccentricity values.

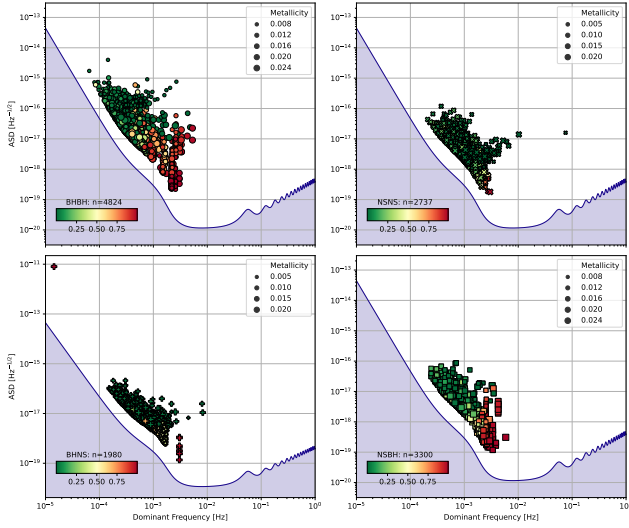


**Figure 2.** Detectable sources' characteristic strain vs. dominant frequency in our simulations are shown on the LISA sensitivity curve for  $\Theta_1$  data set. The sources are color-coded based on their eccentricities, green for low and red for high eccentric sources.

Majority of the binary population reside on the lower end of LISA spectrum. From figure 3 it can be seen that the peak orbital frequency occurs at 0.174 mHz, 0.5308 mHz, 0.3039 mHz, and 0.4016 mHz respectively for BHBBH, NSNS, BHNS and NSBH population, **Row1**. Similarly, in **Row2**, the peak dominant frequency occurs at 0.3919 mHz, 1.057 mHz, 0.5828 mHz, and 0.8668 mHz respectively. **Row3** shows that a large portion of our binaries is either low or mid-eccentric. The orbit of low eccentric binaries evolves differently than high eccentric binaries. After the formation of DCO, the low eccentric binaries emit GW in the second harmonic of their orbital frequency. The intensity of the frequency increases as the orbits starts to shrink. On the other hand, the DCOs with high eccentricities decay faster, and they tend to emit GW in high harmonics (Peters & Mathews 1963; Peters 1964). This also explains why even though the

orbital frequency of the high eccentric binaries was small but they have larger dominant frequency.

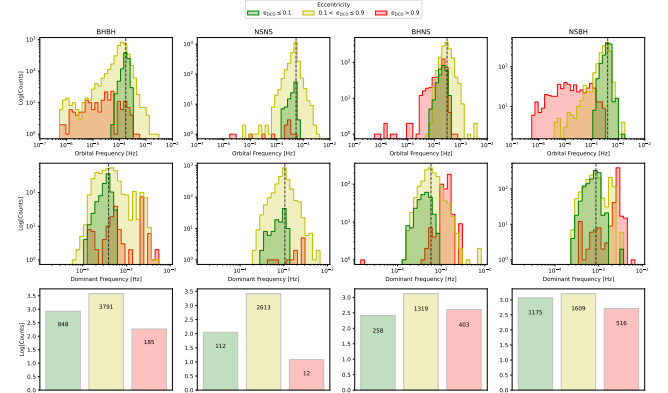


**Figure 3. Row1:** Eccentricity characterized distribution of DCOs for their orbital frequency. **Row2:** Same as **Row1** but for the binary's dominant frequency. **Row3:** Number of binaries associated with the given eccentricity in log scale. The number inside the bars show the actual number of binaries for the given eccentricity. The log scaling was chosen due to relative lower number of DCOs in NSNS and BHNS types.

#### 4.2. A peculiar BHNS binary

We also notice a stray binary pair in BHNS with an  $\text{ASD} \sim 8 \times 10^{-12} \text{ Hz}^{1/2}$ , the highest in  $\Theta_1$ . The parameter of that particular BHNS pair are presented in table 3. It is important to note that before the binary's evolution for SNR detection, it had originally evolved past its lookback time. With a lookback time of  $\sim 10.393$  Myr and evolution time of  $\sim 10.944$  Myr, the merging time for this binary came out to be only  $\sim 3.83$  yr. This also explains why the parameters of this binary are identical when considering the DCO stage and near merging stage after evolving via LEGWORK. The system is emitting a dominant frequency of  $\sim 1.439 \times 10^{-5}$  Hz at a harmonic of 1, which makes it exactly the same as its orbital frequency.

**Table 3.** Parameters at difference stages of binary evolution for BHNS pair with seed number 8848207.

Binary Stage	$m_1$ ( $M_\odot$ )	$m_2$ ( $M_\odot$ )	$a$ (AU)	$e$	$Z$
ZAMS	33.449	17.711	0.666	0.153	0.024
DCO & LISA	6.495	1.407	0.034	0.999	//

<sup>8</sup> [https://matplotlib.org/stable/gallery/color/colormap\\_reference.html](https://matplotlib.org/stable/gallery/color/colormap_reference.html)

### 4.3. Detection within MW components

Figure 4 shows the percentage of different DCOs detected in the low-[ $\alpha/\text{Fe}$ ], high-[ $\alpha/\text{Fe}$ ] and bulge components of the MW instances. For low-[ $\alpha/\text{Fe}$ ] disk, the NSBH pairs have more detections than BHN pairs. Contrary to that, NSBH pairs show no detection in high-[ $\alpha/\text{Fe}$ ] disk, and fractional detection in the bulge,  $\sim 0.833\%$ . On the other hand, the BHNS pairs have the lowest detection rate in all three components.

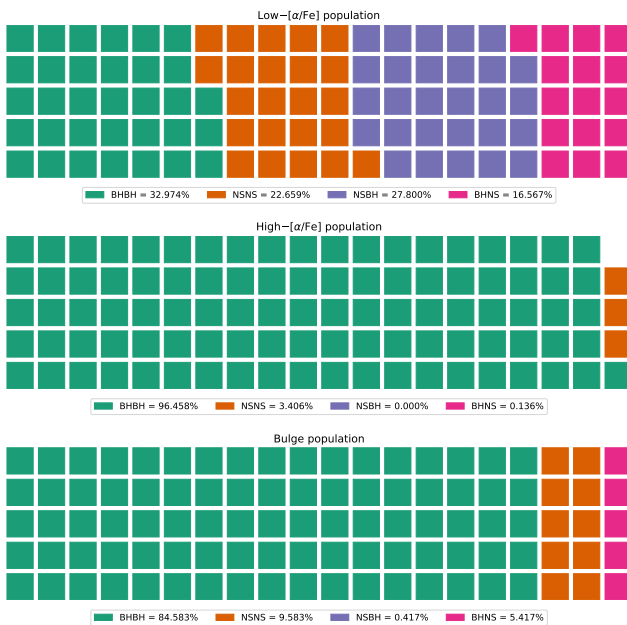


**Figure 4.** Waffle charts showing percentage proportion for DCO type detections in the MW instance components in this study.

BHBH is the dominant detectable pair in all three components. Except for the low-[ $\alpha/\text{Fe}$ ] component, the NSNS pair also has higher percentage of detection. For the low-[ $\alpha/\text{Fe}$ ] component we see a higher percentage of NSBH detection.

Figure 5 shows the percentage of detections in the three components regardless of the DCO type.

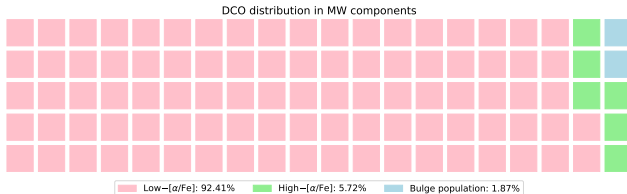


**Figure 5.** Waffle chart showing the total number of detections per MW instance component in this study on the whole.

Here we see that majority of the detections are in the low-[ $\alpha/\text{Fe}$ ] disk. This can be attributed to the biased metallicity value used in this study, Beta(5, 80). These detection percentages do align with the age-metallicity relationship as the bulge is oldest component and thus should have lower metallicity ZAMS stars. However, due to the choice of metallicity distribution, these stars were not generated in large numbers.

### 4.4. Maximum observable distance

For each DCO, there is a horizon distance i.e., the maximum distance up to which the DCO may be detectable in LISA. This is calculated using the inverse relationship between SNR ( $\rho$ ) and distance (Lau et al. 2020),

$$d_{\max} = \frac{\rho(d = 1 \text{ kpc})}{\rho_{\min}} \quad (6)$$

Where  $\rho_{\min}$  is the minimum value of SNR below which the source is not detectable. We keep the detection threshold at  $\rho_{\min} = 7$ , and  $\rho(d = 1 \text{ kpc})$  is SNR of the source if it was at 1 kpc distance from the detector. We calculated the SNR of all the detected sources at 1 kpc distance using the python package LEGWORK (Wagg et al. 2022a). Afterward, their maximum distances ( $d_{\max}$ ) were calculated.

Figure 6 shows the mean maximum distances for all the detected sources. The black line shows the average maximum distance for all the types combined. The LISA sensitivity curve is also overlaid on the graph.

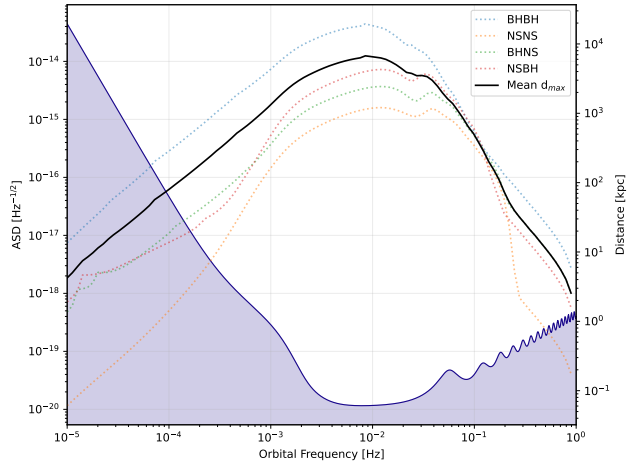


**Figure 6.** Mean maximum distances for all of the different types of DCO corresponding to their orbital frequency. The overall average maximum detection distance is shown by a black line.

BHBH pairs can be observed up to an average distance of  $\sim 19.5$  Mpc. For NSNS, BHNS, and NSBH the maximum distance came out to be  $\sim 1.21$  Mpc,  $\sim 4.28$  Mpc,

and  $\sim 2.43$  Mpc respectively. The combined mean maximum distance comes out to be  $\sim 6.74$  Mpc.

We also observe that the maximum distance for all the binaries is observed around the dominant frequency right around the LISA's most sensitive region, e.g., 10 mHz. For BHBH, the maximum distance is observed at 8.498 mHz. The NSNS, BHNS, and NSBH pairs show the maximum distance value at the same frequency, 12.05 mHz. However, when taking the mean for all four DCO types, the dominant frequency corresponding to the maximum distance changes back to 8.498 mHz showing the effects of the most dominantly detected DCO type, BHBH.

#### 4.5. Two interesting NSNS binaries

Appendix D figure 25 shows a spike in the NSNS SNR plot. This is due to an extremely high value of SNR found in the simulated galaxy number 43, with an average  $\log_{10}(\text{SNR})$  of  $1.6864 \pm 2.7482$ . The maximum SNR in that galaxy is of the binary at seed number 6308709. The particulars of this binary are given in table 4.

**Table 4.** Parameters of NSNS binary with the highest SNR.

$m_{1\text{DCO}}$	$m_{2\text{DCO}}$	$a_{\text{DCO}}$	$e_{\text{DCO}}$
( $M_\odot$ )	( $M_\odot$ )	(AU)	
1.26	1.91	0.044	0.9999
<hr/>			
$Z$	$t_{\text{evol}}$	$t_{\text{lookback}}$	SNR
	(Myr)	(Myr)	
0.02595	30.135	4.967	$6.8467 \times 10^{14}$

**Table 5.** LISA parameters for binary with  $\phi = 1699345$  obtained by LEGWORK before SNR calculations.

LISA parameters for $\phi = 1699345$			
$f_{\text{orb}}$	ASD	$a_{\text{LISA}}$	$e_{\text{LISA}}$
(mHz)	( $10^{-17} \text{ Hz}^{-1/2}$ )	( $R_\odot$ )	
1	27.318	2.611	35.384
2	52.504	3.155	22.890
3	255.01	1.236	7.981
			0.4175
			0.2601
			0.0554

Upon further investigations, we came to know that the binary might have merged already. The LISA pa-

rameters,  $e_{\text{LISA}}, a_{\text{LISA}}, f_{\text{LISA}}$ , for said binary show that the semi-major axis and eccentricity for this binary at the time of SNR detection are  $8.66 \times 10^{-51}$  AU and  $10.34 \times 10^{-72}$  respectively. The extremely high SNR also accompanies an equally high dominant frequency, out of the plotting range, of roughly  $1.4 \times 10^{68}$  Hz and an undefined ASD value.

We show the detections of  $\Theta_2$  is figure 7. The binary discussed above, with seed number 6308709, is not visible in this plot. However, there are three more NSNS detections that are out of characteristics with high dominant frequencies, and all three are the same pair with seed number 1699345. The particulars of this binary are presented in table 5.

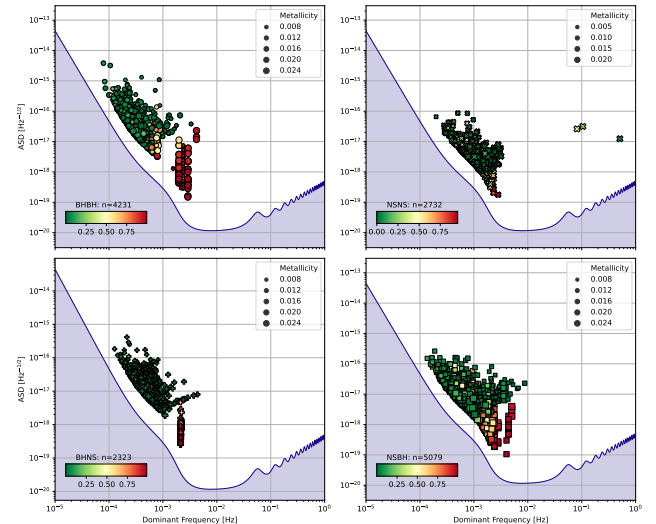


**Figure 7.** Same as figure 2 but for  $\Theta_2$  data set.

#### 4.6. Final evolutionary stages

A total of 137 seeds were found common between the two data sets. Out of these 137 seeds, 104 were found to evolve to the same final stage in both data sets. The binaries with common and diverging final evolutionary stages are shown in figure 8. The lesser number of diverging cases indicate that the ZAMS eccentricity might not play as much of a bigger role in the development of binary's final stages.

For a better understanding of what the plot is showing, consider the two points highlighted. The red marker on the tail of the arrow shows the DCO stage for the binary in  $\Theta_1$  data set, the arrow indicates direction of divergence in evolution with the arrow head showing the final DCO stage of the same binary in  $\Theta_2$  data set. On the other hand, the cyan marker indicates no divergence in the evolution, meaning that the binary had the same

final evolution stage in both the data sets. The particular binaries in question have seed numbers, 44735 and 1367057 respectively.

## 5. ACKNOWLEDGMENTS

The authors thank the Space and Astrophysics Research Lab (SARL) and the National Center of GIS and Space Applications (NCGSA) for the computational facilities provided that helped with this project. Bukhari also thanks the COMPAS collaborations that provided help and clarification on the selection of NS evolution model. Also, a special thanks to Tom Wagg for the helpful discussions on the LEGWORK working and the galaxy models provided for the synthesis.

We made use of the COMPAS suite (Riley et al. 2022) for the initial binary simulation. These binaries were and later further evolved using LEGWORK (Wagg et al. 2022a) to calculate their S/N ratio for LISA detection.

The research also uses several open source software like, Python (v3.9.7) via the `miniconda` installer available at the miniconda website.<sup>9</sup> Additionally, the packages NumPy (Harris et al. 2020), `matplotlib` (Barrett et al. 2005; Hunter 2007), `astropy` (Astropy Collaboration et al. 2013), `pandas` (Reback et al. 2021), `seaborn` (Waskom 2021), `h5py` (Collette et al. 2018, 2021), `scipy` (Virtanen et al. 2020) and more were used.

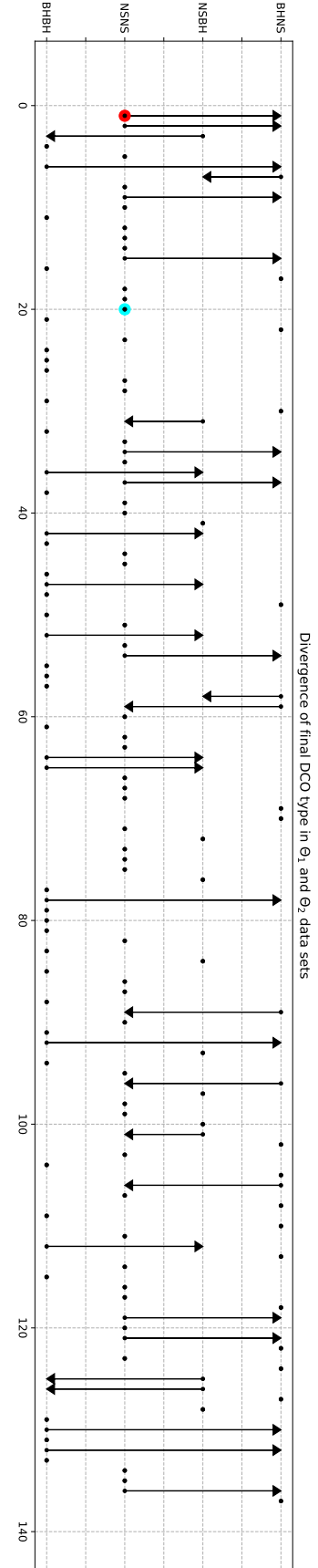


**Figure 8.** Plot showing the change in DCO ending states for the common seed numbers from  $\Theta_1$  and  $\Theta_2$  data sets. The direction of arrows shows the change in the DCO type from  $\Theta_1$  and  $\Theta_2$  data set. The binaries that didn't change the DCO type after evolution are represented by a filled dot.

<sup>9</sup> <https://docs.conda.io/en/latest/miniconda.html>

## APPENDIX

## A. SETTINGS FOR USING COMPAS

To generate a binary systems, COMPAS requires the following parameters from the user as discussed earlier,

- mass of primary star ( $m_{1\text{ZAMS}}$ ),
- mass of secondary star ( $m_{2\text{ZAMS}}$ ),
- semi-major axis of the orbit ( $a_{\text{ZAMS}}$ ),
- random seed ( $\phi$ )
- remnant mass prescription,
- eccentricity of the orbit ( $e_{\text{ZAMS}}$ ), and
- metallicity of the stars ( $Z$ ).

We've discussed the first four parameters in the main text, here we will discuss the selection of eccentricity and metallicity values.

## A.1. Eccentricity

In order to evaluate whether the initial eccentricity affects GW emission at the end stages of the DCO, we generate two identical data sets. For the primary data set, we chose the eccentricity value to be varied between 0 and 1.

However, we noticed that some stars within the population synthesis had a ZAMS stellar type of 16. This refers to chemically homogeneously evolving stars (Riley et al. 2021, 2022). These binaries were found to have zero eccentricity even when the parameter was chosen to be within the range  $(0, 1]$ .

For the other data set we take the eccentricity value to be 0 for all the generated binaries.

## A.2. Metallicity

One of the major challenges in generation of the stellar binaries for this study was the selection of a distribution which will result in stars at the higher end of COMPAS metallicity boundary,  $z = 0.03$ . A power-law, gamma, and beta distributions were selected to try and simulate the required metallicity distribution. In the following section, we discuss the selected distributions briefly,

*Power law distribution*—The random values for metallicity were generated using the power law distribution given below,

$$f(x, a) = ax^{(a-1)} \quad (\text{A1})$$

where  $a$  is the index of the power law distribution.<sup>10</sup> Figure 9 (a) shows the plot for the probability density function (PDF) of the power law with  $a \in [1, 2]$ . Although the distribution can produce higher values, it does not suppress the lower values so this distribution was discarded.

*Gamma distribution*—For the probability density function for gamma distribution,<sup>11</sup> we use the following form,

$$f(x, a) = \frac{x^{a-1} \exp(-x)}{\Gamma(a)} \quad (\text{A2})$$

for  $x \geq 0$  and  $a > 0$ . Here,  $a$  is the shape factor, and  $\Gamma$  is the gamma function, such that  $\Gamma(a) = (a - 1)!$ . Similar to the power law distribution, the gamma distribution, figure 9 (b), was not a good selection for the values of metallicity that were required for this study.

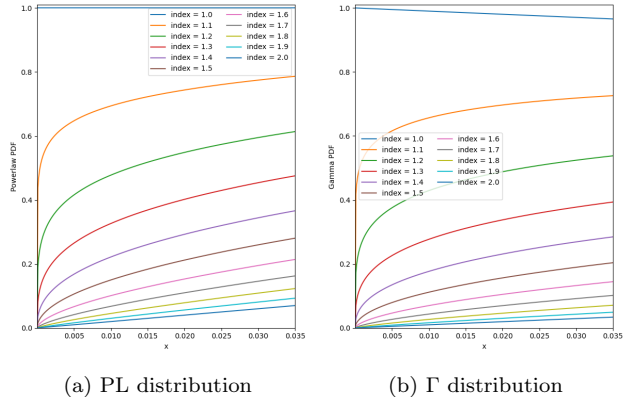


**Figure 9.** Implementation of (a) Power Law and (b)  $\Gamma$  distribution using various indices

*Beta distribution*—For the beta distribution, we use the following form,

$$f(x, a, b) = \frac{\Gamma(a + b)x^{a-1}(1 - x)^{b-1}}{\Gamma(a)\Gamma(b)} \quad (\text{A3})$$

For  $0 \leq x \leq 1, a > 0, b > 0$  and  $\Gamma$  is the gamma function.<sup>12</sup>

<sup>10</sup> <https://docs.scipy.org/doc/scipy/reference/generated/scipy.stats.powerlaw.html>

<sup>11</sup> <https://docs.scipy.org/doc/scipy/reference/generated/scipy.stats.gamma.html>

<sup>12</sup> <https://docs.scipy.org/doc/scipy/reference/generated/scipy.stats.beta.html>

Figure 10 (a) shows the beta distribution with a fixed  $\beta = 80$ . Similarly, figure 10 (b) shows the beta distribution with a fixed  $\alpha = 5$ . For our case, we selected Beta(5, 80) as our distribution of choice for metallicity and generated  $10^7$  values between the COMPAS limits  $10^{-4} < z < 0.03$ .

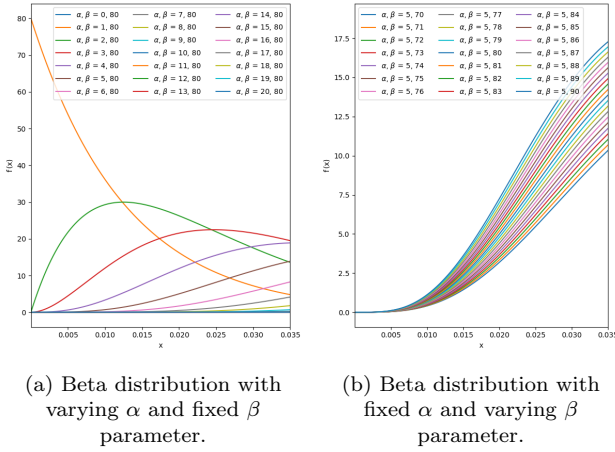


**Figure 10.** Implementation of Beta distribution using differing indices for  $\alpha$  and  $\beta$  parameters.

The same value for metallicity were used for both stars as different metallicity scenario is highly unlikely.

## B. THE MILKY WAY MODEL

In this section, we will briefly outline the milky way galaxy model used in this study. The model is developed by Wagg et al. (2022a) and makes use of the galaxy's enrichment history by taking into account the metallicity-radius-time relationship (Frankel et al. 2018). It uses a separate star formation history and spatial distribution for the low-[ $\alpha/\text{Fe}$ ], high-[ $\alpha/\text{Fe}$ ] discs, and bulge in the galaxy.

### B.1. Star formation rate

The star formation rate for both the low-[ $\alpha/\text{Fe}$ ] and high-[ $\alpha/\text{Fe}$ ] disks is expressed as,

$$p(\tau) \propto \exp\left(-\frac{\tau_m - \tau}{\tau_{\text{SFR}}}\right), \quad (\text{B4})$$

where  $\tau$  is the time difference between the star's ZAMS stage and today. The age of milky way galaxy,  $\tau_m$ , is taken as 12 Gyr, and the star formation rate as,  $\tau_{\text{SFR}} = 6.8$  Gyr. The star-forming period of low-[ $\alpha/\text{Fe}$ ] and high-[ $\alpha/\text{Fe}$ ] discs were taken as 0 Gyr to 8 Gyr and 8 Gyr to 12 Gyr respectively. The model adopts 6 Gyr to 12 Gyr as the star-forming period of the bulge (Bovy et al. 2019).

### B.2. Radial distribution

The radial distribution of stars within the milky way galaxy was performed using the following expression,

$$p(R) = \exp\left(-\frac{R}{R_d}\right) \frac{R}{R_d^2} \quad (\text{B5})$$

However, a different scale length,  $R_d$ , was chosen for each component of the galaxy. For low-[ $\alpha/\text{Fe}$ ], the model uses  $R_{\text{exp}}(\tau)$  as the scale length (Frankel et al. 2018, Eq 6), where

$$R_{\text{exp}}(\tau) = 4 \text{ kpc} \left[ 1 - \alpha_{R_{\text{exp}}} \left( \frac{\tau}{8 \text{ Gyr}} \right) \right], \quad (\text{B6})$$

with the value of inside-out growth parameter,  $\alpha_{R_{\text{exp}}}$ , as 0.3. For high-[ $\alpha/\text{Fe}$ ] disc and bulge, the value of scale length was chosen as  $(1/0.43)$  kpc and 1.5 kpc respectively.

### B.3. Vertical distribution

The model employs a similar method of single exponent expression with varying scale height parameters for the vertical distribution as well. The exponential expression used is,

$$p(|z|) = \frac{1}{z_d} \exp\left(-\frac{|z|}{z_d}\right), \quad (\text{B7})$$

where  $z$  here is the vertical displacement from the galactic plane. The scale height parameter,  $z_d$ , for low-[ $\alpha/\text{Fe}$ ], high-[ $\alpha/\text{Fe}$ ] and bulge was taken as 0.3 kpc McMillan (2011), 0.95 kpc Bovy et al. (2016), and 0.2 kpc Wegg et al. (2015) respectively.

### B.4. Metallicity-radius-time relationship

The MRT relationship plays an important part, both in the galaxy model and later on in the placement of DCOs within the galaxy as well. The model makes use of (Frankel et al. 2018, Eq. 7),

$$[\text{Fe}/\text{H}](R, \tau) = F_m + \nabla[\text{Fe}/\text{H}]R - (F_m + \nabla[\text{Fe}/\text{H}]R_{[\text{Fe}/\text{H}=0]}^{\text{now}})f(\tau) \quad (\text{B8})$$

$$\nabla[\text{Fe}/\text{H}]R_{[\text{Fe}/\text{H}=0]}^{\text{now}} \quad (\text{B9})$$

For each point generated, if the value of metallicity produced by the MW model was less or greater than the limits defined by COMPAS<sup>13</sup> it was changed to a uniformly drawn random number between  $\text{COMPAS}_{\min} - \text{ZSOLAR}$  and  $\text{ZSOLAR} - \text{COMPAS}_{\max}$  respectively.

<sup>13</sup> 0.0001, 0.03

### B.5. Galaxy synthesis

For the synthesis of an instance of the Milky Way galaxy, the model described previously samples the following parameters,

$$\theta_i = \{\tau, D, z, \text{component}\},$$

where  $\tau$  is the look-back time for the binary,  $D$  is the distance from Earth,  $z$  is the metallicity, and ‘component’ is the component of the galaxy in which the binary resides.<sup>14</sup> The parameters are generated for  $i = 1, 2, 3, \dots, N_{\text{GAL}}$ , where  $N_{\text{GAL}} = 100$ .

## C. PARAMETER DISTRIBUTION ACROSS THE GALAXIES – $\Theta_1$

### C.1. Binary Black Holes

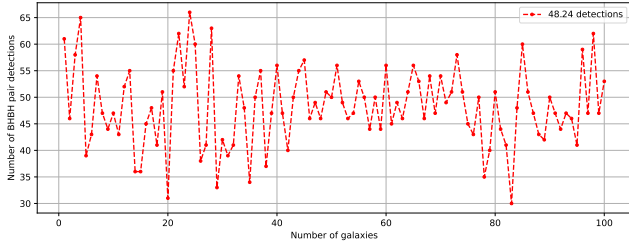


**Figure 11.** Number of BHBH pair detection per galaxy instance. On average, a total of  $\sim 48$  pairs per galaxy were detected in this study.

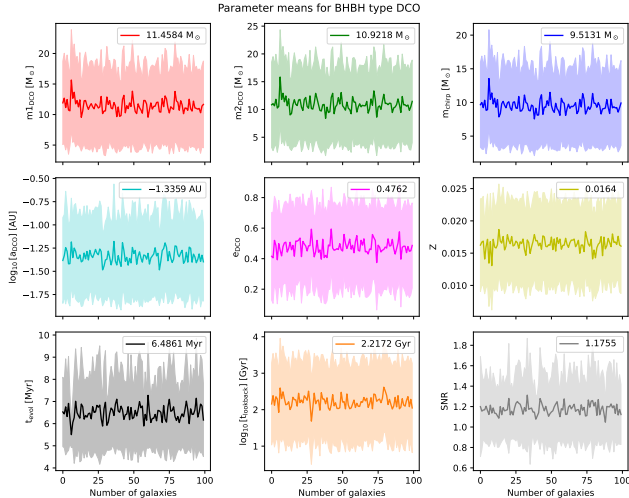


**Figure 12.** The mean and standard deviation for selected parameters in every galaxy, plotted against the galaxy number. An overall measure of mean and standard deviation of all the galaxies is also shown for the selected parameters.

### C.2. Binary Neutron Stars

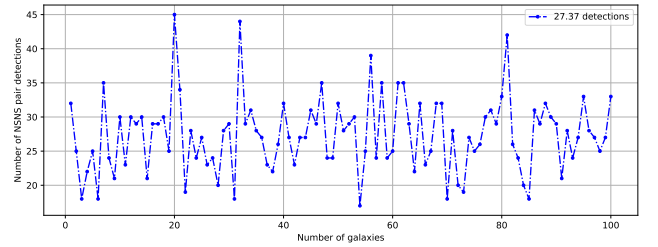


**Figure 13.** Number of NSNS pair detection per galaxy instance. On average, a total of  $\sim 27$  pairs per galaxy were detected in this study.

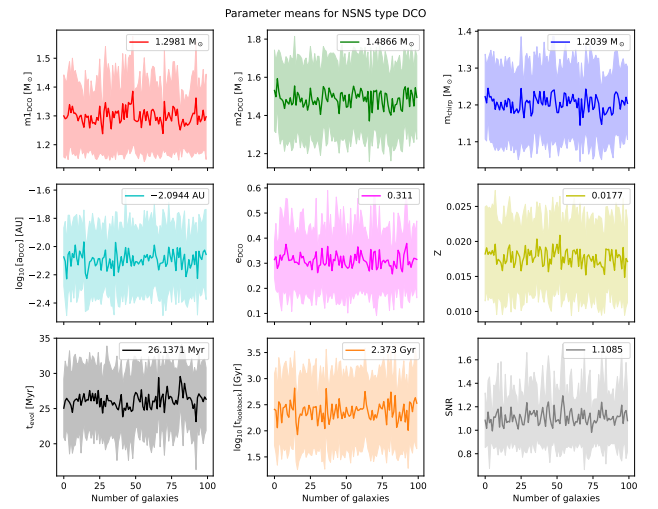


**Figure 14.** Same as figure 12.

### C.3. Black Hole – Neutron Star binary

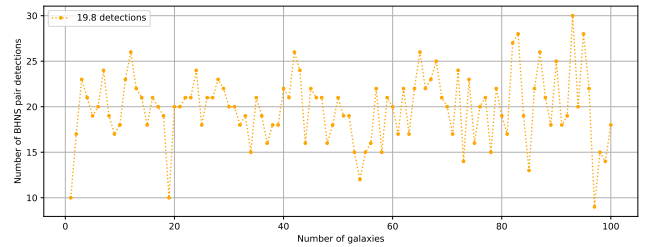


**Figure 15.** Number of BHNS pair detection per galaxy instance. On average, a total of  $\sim 20$  pairs per galaxy were detected in this study.

<sup>14</sup> One of the three, low-[ $\alpha$ /Fe] disc, high-[ $\alpha$ /Fe] disc, or bulge.

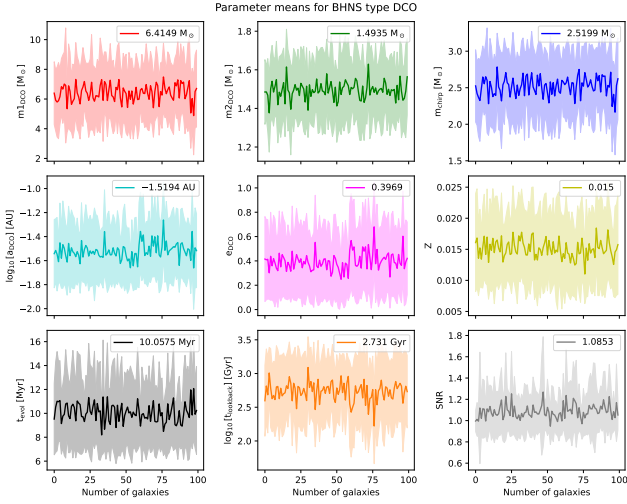


**Figure 16.** Same as figure 12.

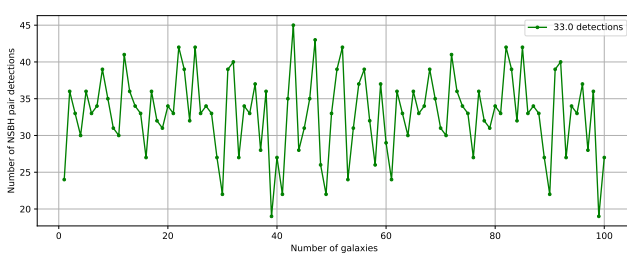


**Figure 17.** Number of NSBH pair detection per galaxy instance. On average, a total of  $\sim 33$  pairs per galaxy were detected in this study.

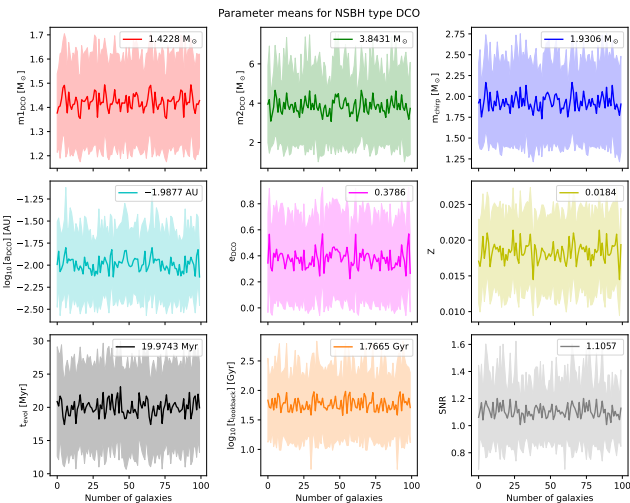


**Figure 18.** Same as figure 12.

#### C.4. Neutron Star – Black Hole binary

### D. PARAMETER DISTRIBUTION ACROSS THE GALAXIES – $\Theta_2$

#### D.1. Binary Black Holes

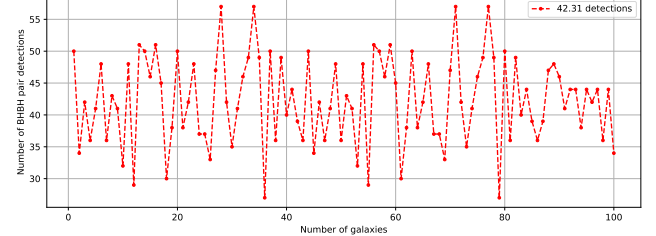


**Figure 19.** Number of BHBH pair detection per galaxy instance. On average, a total of  $\sim 42$  pairs per galaxy were detected in this study.

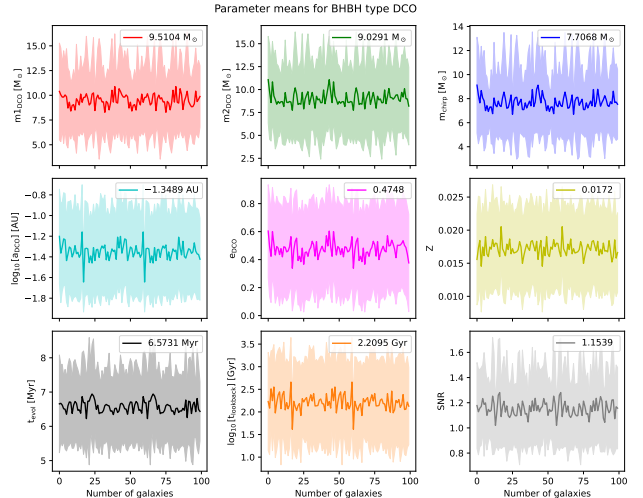


**Figure 20.** The mean and standard deviation for selected parameters in every galaxy, plotted against the galaxy number. An overall measure of mean and standard deviation of all the galaxies is also shown for the selected parameters.

#### D.2. Binary Neutron Stars

#### D.3. Black Hole – Neutron Star binary

#### D.4. Neutron Star – Black Hole binary

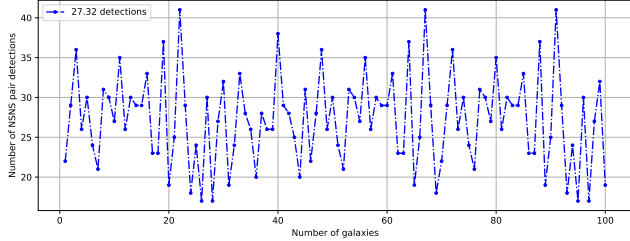


**Figure 21.** Number of NSNS pair detection per galaxy instance. On average, a total of  $\sim 27$  pairs per galaxy were detected in this study.

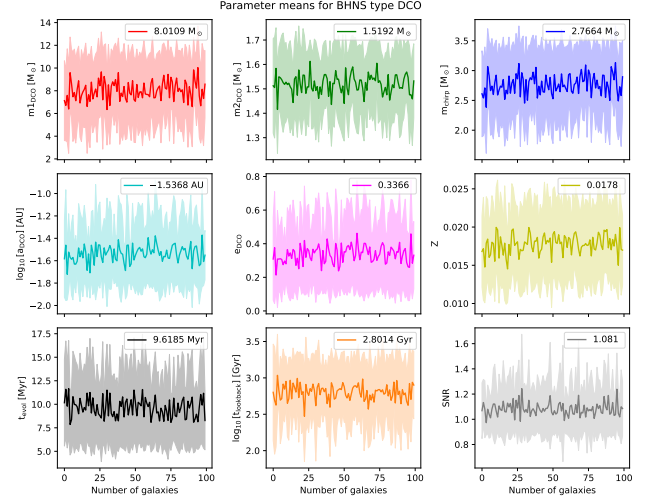


**Figure 24.** Same as figure 20.

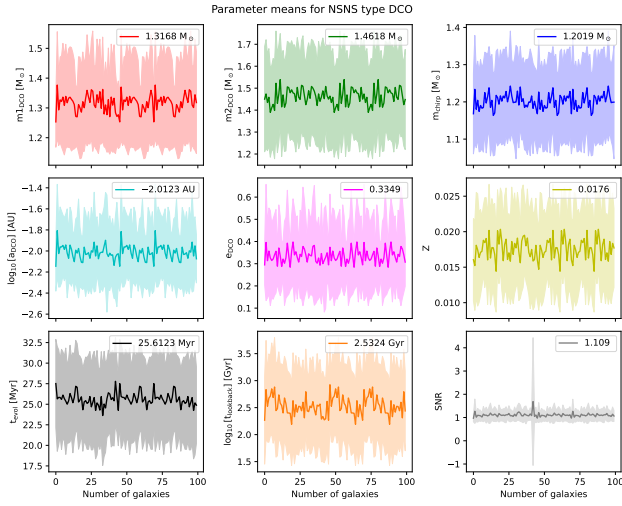


**Figure 22.** Same as figure 20.

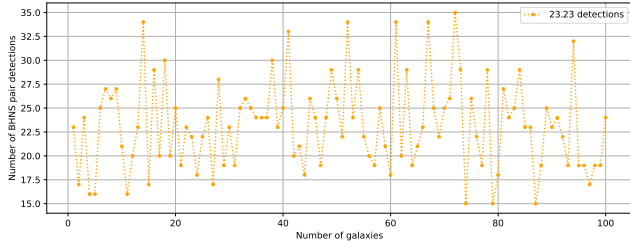


**Figure 23.** Number of BHNS pair detection per galaxy instance. On average, a total of  $\sim 23$  pairs per galaxy were detected in this study.

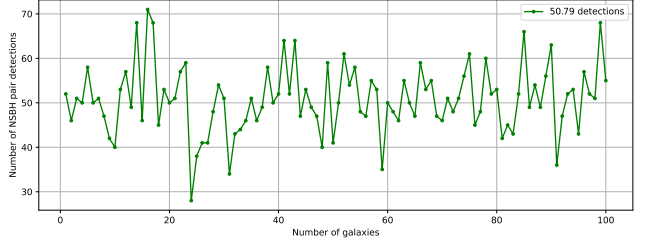


**Figure 25.** Number of NSBH pair detection per galaxy instance. On average, a total of  $\sim 51$  pairs per galaxy were detected in this study.

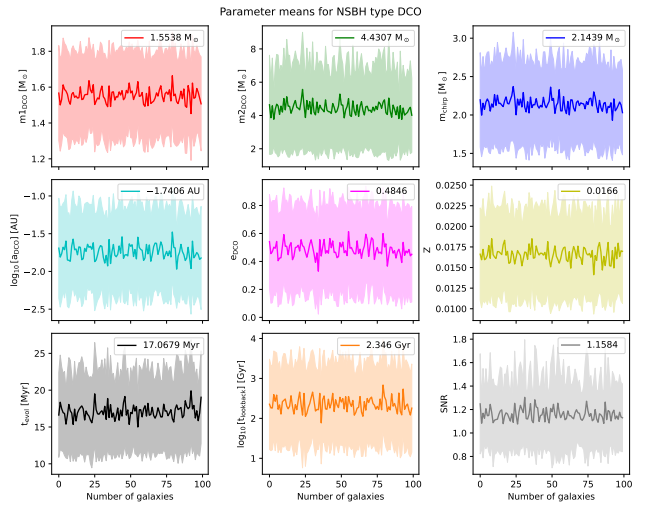


**Figure 26.** Same as figure 20.

## REFERENCES

- Abbott, B. P., Abbott, R., Abbott, T. D., et al. 2016, PhRvL, 116, 061102, doi: [10.1103/PhysRevLett.116.061102](https://doi.org/10.1103/PhysRevLett.116.061102)
- Acernese, F., Agathos, M., Agatsuma, K., et al. 2015, Classical and Quantum Gravity, 32, 024001. <https://arxiv.org/abs/1408.3978>
- Andrews, J. J., Breivik, K., Pankow, C., D’Orazio, D. J., & Safarzadeh, M. 2020, ApJL, 892, L9, doi: [10.3847/2041-8213/ab5b9a](https://doi.org/10.3847/2041-8213/ab5b9a)
- Astropy Collaboration, Robitaille, T. P., Tollerud, E. J., et al. 2013, A&A, 558, A33, doi: [10.1051/0004-6361/201322068](https://doi.org/10.1051/0004-6361/201322068)
- Babak, S., Baker, J. G., Benacquista, M. J., et al. 2008, Classical and Quantum Gravity, 25, 114037, doi: [10.1088/0264-9381/25/11/114037](https://doi.org/10.1088/0264-9381/25/11/114037)
- . 2010, Classical and Quantum Gravity, 27, 084009, doi: [10.1088/0264-9381/27/8/084009](https://doi.org/10.1088/0264-9381/27/8/084009)
- Barack, L., & Cutler, C. 2004, PhRvD, 69, 082005, doi: [10.1103/PhysRevD.69.082005](https://doi.org/10.1103/PhysRevD.69.082005)
- Barrett, P., Hunter, J., Miller, J. T., Hsu, J. C., & Greenfield, P. 2005, in Astronomical Society of the Pacific Conference Series, Vol. 347, Astronomical Data Analysis Software and Systems XIV, ed. P. Shopbell, M. Britton, & R. Ebert, 91
- Belczynski, K., Benacquista, M., & Bulik, T. 2010, ApJ, 725, 816, doi: [10.1088/0004-637X/725/1/816](https://doi.org/10.1088/0004-637X/725/1/816)
- Błaut, A., Babak, S., & Królak, A. 2010, PhRvD, 81, 063008, doi: [10.1103/PhysRevD.81.063008](https://doi.org/10.1103/PhysRevD.81.063008)
- Bovy, J., Leung, H. W., Hunt, J. A. S., et al. 2019, MNRAS, 490, 4740, doi: [10.1093/mnras/stz2891](https://doi.org/10.1093/mnras/stz2891)
- Bovy, J., Rix, H.-W., Schlaflay, E. F., et al. 2016, ApJ, 823, 30, doi: [10.3847/0004-637X/823/1/30](https://doi.org/10.3847/0004-637X/823/1/30)
- Broekgaarden, F. S., Justham, S., de Mink, S. E., et al. 2019, MNRAS, 490, 5228, doi: [10.1093/mnras/stz2558](https://doi.org/10.1093/mnras/stz2558)
- Broekgaarden, F. S., Berger, E., Neijssel, C. J., et al. 2021, MNRAS, 508, 5028, doi: [10.1093/mnras/stab2716](https://doi.org/10.1093/mnras/stab2716)
- Chapman-Bird, C. E. A., Berry, C. P. L., & Woan, G. 2022, arXiv e-prints, arXiv:2212.06166, doi: [10.48550/arXiv.2212.06166](https://doi.org/10.48550/arXiv.2212.06166)
- Collette, A., Tocknell, J., Caswell, T. A., et al. 2018, H5Py/H5Py 2.8.0, 2.8.0, Zenodo, Zenodo, doi: [10.5281/zenodo.1246321](https://doi.org/10.5281/zenodo.1246321)
- Collette, A., Kluyver, T., Caswell, T. A., et al. 2021, h5py/h5py: 3.2.1, 3.2.1, Zenodo, Zenodo, doi: [10.5281/zenodo.4584676](https://doi.org/10.5281/zenodo.4584676)
- Digman, M. C., & Hirata, C. M. 2022, arXiv e-prints, arXiv:2212.14887, doi: [10.48550/arXiv.2212.14887](https://doi.org/10.48550/arXiv.2212.14887)
- Eddington, A. S. 1922, Proceedings of the Royal Society of London Series A, 102, 268, doi: [10.1098/rspa.1922.0085](https://doi.org/10.1098/rspa.1922.0085)
- Einstein, A. 1916, Sitzungsberichte der Königlich Preußischen Akademie der Wissenschaften (Berlin), 688
- Finn, L. S., & Thorne, K. S. 2000, PhRvD, 62, 124021, doi: [10.1103/PhysRevD.62.124021](https://doi.org/10.1103/PhysRevD.62.124021)
- Frankel, N., Rix, H.-W., Ting, Y.-S., Ness, M., & Hogg, D. W. 2018, ApJ, 865, 96, doi: [10.3847/1538-4357/aadba5](https://doi.org/10.3847/1538-4357/aadba5)
- Fryer, C. L., Belczynski, K., Wiktorowicz, G., et al. 2012, ApJ, 749, 91, doi: [10.1088/0004-637X/749/1/91](https://doi.org/10.1088/0004-637X/749/1/91)
- Fumagalli, J., Pieroni, M., Renaux-Petel, S., & Witkowski, L. T. 2022, JCAP, 2022, 020, doi: [10.1088/1475-7516/2022/07/020](https://doi.org/10.1088/1475-7516/2022/07/020)
- Gair, J. R., Babak, S., Sesana, A., et al. 2017, in Journal of Physics Conference Series, Vol. 840, Journal of Physics Conference Series, 012021, doi: [10.1088/1742-6596/840/1/012021](https://doi.org/10.1088/1742-6596/840/1/012021)
- Guo, H.-K., Shu, J., & Zhao, Y. 2017, arXiv e-prints, arXiv:1709.03500. <https://arxiv.org/abs/1709.03500>
- Harris, C. R., Millman, K. J., van der Walt, S. J., et al. 2020, Nature, 585, 357, doi: [10.1038/s41586-020-2649-2](https://doi.org/10.1038/s41586-020-2649-2)
- Hulse, R. A., & Taylor, J. H. 1975, ApJL, 195, L51, doi: [10.1086/181708](https://doi.org/10.1086/181708)
- Hunter, J. D. 2007, Computing in Science and Engineering, 9, 90, doi: [10.1109/MCSE.2007.55](https://doi.org/10.1109/MCSE.2007.55)
- Hurley, J. R., Pols, O. R., & Tout, C. A. 2000, MNRAS, 315, 543, doi: [10.1046/j.1365-8711.2000.03426.x](https://doi.org/10.1046/j.1365-8711.2000.03426.x)
- Hurley, J. R., Tout, C. A., & Pols, O. R. 2002, MNRAS, 329, 897, doi: [10.1046/j.1365-8711.2002.05038.x](https://doi.org/10.1046/j.1365-8711.2002.05038.x)
- Khakhaleva-Li, Z., & Hogan, C. J. 2020, arXiv. <https://arxiv.org/abs/2006.00438>
- Klein, A., Barausse, E., Sesana, A., et al. 2016, PhRvD, 93, 024003, doi: [10.1103/PhysRevD.93.024003](https://doi.org/10.1103/PhysRevD.93.024003)
- Korol, V., Rossi, E. M., & Groot, P. J. 2017, in Astronomical Society of the Pacific Conference Series, Vol. 509, 20th European White Dwarf Workshop, ed. P. E. Tremblay, B. Gaensicke, & T. Marsh, 529
- Kroupa, P. 2001, MNRAS, 322, 231, doi: [10.1046/j.1365-8711.2001.04022.x](https://doi.org/10.1046/j.1365-8711.2001.04022.x)
- Lau, M. Y. M., Mandel, I., Vigna-Gómez, A., et al. 2020, MNRAS, 492, 3061, doi: [10.1093/mnras/staa002](https://doi.org/10.1093/mnras/staa002)
- LIGO Scientific Collaboration, Aasi, J., Abbott, B. P., et al. 2015, Classical and Quantum Gravity, 32, 074001, doi: [10.1088/0264-9381/32/7/074001](https://doi.org/10.1088/0264-9381/32/7/074001)
- Mandel, I., & Müller, B. 2020, MNRAS, 499, 3214, doi: [10.1093/mnras/staa3043](https://doi.org/10.1093/mnras/staa3043)
- McMillan, P. J. 2011, MNRAS, 414, 2446, doi: [10.1111/j.1365-2966.2011.18564.x](https://doi.org/10.1111/j.1365-2966.2011.18564.x)
- Nelemans, G., Yungelson, L. R., & Portegies Zwart, S. F. 2001, A&A, 375, 890, doi: [10.1051/0004-6361:20010683](https://doi.org/10.1051/0004-6361:20010683)

- Öpik, E. 1924, Publications of the Tartu Astrofizica Observatory, 25, 1
- Peters, P. C. 1964, Physical Review, 136, 1224, doi: [10.1103/PhysRev.136.B1224](https://doi.org/10.1103/PhysRev.136.B1224)
- Peters, P. C., & Mathews, J. 1963, Physical Review, 131, 435, doi: [10.1103/PhysRev.131.435](https://doi.org/10.1103/PhysRev.131.435)
- Prince, T. A., Tinto, M., Larson, S. L., & Armstrong, J. W. 2002, PhRvD, 66, 122002, doi: [10.1103/PhysRevD.66.122002](https://doi.org/10.1103/PhysRevD.66.122002)
- Reback, J., Jbrockmendel, McKinney, W., et al. 2021, pandas-dev/pandas: Pandas 1.3.0, v1.3.0, Zenodo, Zenodo, doi: [10.5281/zenodo.5060318](https://doi.org/10.5281/zenodo.5060318)
- Renzo, M., Callister, T., Chatzioannou, K., et al. 2021, ApJ, 919, 128, doi: [10.3847/1538-4357/ac1110](https://doi.org/10.3847/1538-4357/ac1110)
- Riley, J., Mandel, I., Marchant, P., et al. 2021, MNRAS, 505, 663, doi: [10.1093/mnras/stab1291](https://doi.org/10.1093/mnras/stab1291)
- Riley, J., Agrawal, P., Barrett, J. W., et al. 2022, ApJS, 258, 34, doi: [10.3847/1538-4365/ac416c](https://doi.org/10.3847/1538-4365/ac416c)
- Robson, T., Cornish, N. J., & Liu, C. 2019, Classical and Quantum Gravity, 36, 105011, doi: [10.1088/1361-6382/ab1101](https://doi.org/10.1088/1361-6382/ab1101)
- Ruiter, A. J., Belczynski, K., Benacquista, M., Larson, S. L., & Williams, G. 2010, ApJ, 717, 1006, doi: [10.1088/0004-637X/717/2/1006](https://doi.org/10.1088/0004-637X/717/2/1006)
- Sana, H., de Mink, S. E., de Koter, A., et al. 2012, Science, 337, 444, doi: [10.1126/science.1223344](https://doi.org/10.1126/science.1223344)
- Sesana, A., Volonteri, M., & Haardt, F. 2009, Classical and Quantum Gravity, 26, 094033, doi: [10.1088/0264-9381/26/9/094033](https://doi.org/10.1088/0264-9381/26/9/094033)
- Shao, Y., & Li, X.-D. 2021, ApJ, 920, 81, doi: [10.3847/1538-4357/ac173e](https://doi.org/10.3847/1538-4357/ac173e)
- Stevenson, S., Vigna-Gómez, A., Mandel, I., et al. 2017, Nat. Commun., 8, 14906, doi: [10.1038/ncomms14906](https://doi.org/10.1038/ncomms14906)
- Taylor, J. H., & Weisberg, J. M. 1982, ApJ, 253, 908, doi: [10.1086/159690](https://doi.org/10.1086/159690)
- Vigna-Gómez, A., Neijssel, C. J., Stevenson, S., et al. 2018, MNRAS, 481, 4009, doi: [10.1093/mnras/sty2463](https://doi.org/10.1093/mnras/sty2463)
- Virtanen, P., Gommers, R., Oliphant, T. E., et al. 2020, Nature Methods, 17, 261, doi: [10.1038/s41592-019-0686-2](https://doi.org/10.1038/s41592-019-0686-2)
- Wagg, T., Breivik, K., & de Mink, S. E. 2022a, ApJS, 260, 52, doi: [10.3847/1538-4365/ac5c52](https://doi.org/10.3847/1538-4365/ac5c52)
- Wagg, T., Broekgaarden, F. S., de Mink, S. E., et al. 2022b, ApJ, 937, 118, doi: [10.3847/1538-4357/ac8675](https://doi.org/10.3847/1538-4357/ac8675)
- Waskom, M. 2021, The Journal of Open Source Software, 6, 3021, doi: [10.21105/joss.03021](https://doi.org/10.21105/joss.03021)
- Wegg, C., Gerhard, O., & Portail, M. 2015, MNRAS, 450, 4050, doi: [10.1093/mnras/stv745](https://doi.org/10.1093/mnras/stv745)
- Willemse, B., Kalogera, V., Vecchio, A., et al. 2007, ApJL, 665, L59, doi: [10.1086/521049](https://doi.org/10.1086/521049)
- Yu, S., & Jeffery, C. S. 2010, A&A, 521, A85, doi: [10.1051/0004-6361/201014827](https://doi.org/10.1051/0004-6361/201014827)